Raman spectroscopy study of damage in swift heavy ion-irradiated ceramics

Jean-Marc Costantini, Gaelle Gutierrez, Gérald Lelong, Maxime Guillaumet, Md. Majidur Rahman, Kazuhiro Yasuda

▶ **To cite this version:**

Jean-Marc Costantini, Gaelle Gutierrez, Gérald Lelong, Maxime Guillaumet, Md. Majidur Rahman, et al.. Raman spectroscopy study of damage in swift heavy ion-irradiated ceramics. Journal of Raman Spectroscopy, 2022, 53, pp.1614-1624. 10.1002/jrs.6414 . cea-04151155

HAL Id: cea-04151155
https://cea.hal.science/cea-04151155

Submitted on 4 Jul 2023

HAL is a multi-disciplinary open access archive for the deposit and dissemination of scientific research documents, whether they are published or not. The documents may come from teaching and research institutions in France or abroad, or from public or private research centers.

L'archive ouverte pluridisciplinaire **HAL**, est destinée au dépôt et à la diffusion de documents scientifiques de niveau recherche, publiés ou non, émanant des établissements d'enseignement et de recherche français ou étrangers, des laboratoires publics ou privés.

Distributed under a Creative Commons Attribution - NonCommercial - NoDerivatives 4.0 International License

RAMAN SPECTROSCOPY STUDY OF DAMAGE IN SWIFT HEAVY ION-IRRADIATED CERAMICS

Jean-Marc COSTANTINI[1],

Université Paris-Saclay, CEA, Service de Recherches Métallurgiques Appliquées, 91191, Gif-sur Yvette, France

Sandrine MIRO, Gaëlle GUTIERREZ,

Université Paris-Saclay, CEA, Service de Recherches de Métallurgie Physique, 91191, Gif-sur-Yvette, France

Gérald LELONG, Maxime Guillaumet,

Sorbonne Université, Muséum National d'Histoire Naturelle, UMR CNRS 7590, IRD, Institut de Minéralogie, de Physique des Matériaux et de Cosmochimie, IMPMC, 75005 Paris, France

Seiya TAKAKI, Norito ISHIKAWA, Nuclear Science and Engineering Center, Japan Atomic Energy Agency (JAEA), Shirakata 2-4, Tokai, Ibaraki 319-1195, Japan

and Kazuhiro YASUDA,

Department of Applied Quantum Physics and Nuclear Engineering, Kyushu University, 744 Motooka, Nishi-ku, Fukuoka, 819-0395 Japan

ABSTRACT

Raman scattering is applied to probe the radiation damage in swift heavy ion-irradiated ceramics, namely zirconium nitride (ZrN), ceria (CeO_2), and yttria-stabilized zirconia (ZrO_2: Y, or YSZ) for about the same high electronic stopping powers of heavy ions. Raman spectra show that those ceramics

[1] Corresponding author's email : jean-marc.costantini@cea.fr

are radiation-resistant materials which are not amorphized by such irradiations even for large track overlap at high fluences. However, the increase of the TA/LA and TO/LO band intensities versus fluence is evidenced after 100-MeV Xe ion irradiation of ZrN up to a saturation for the fluence of $3x10^{12}$ cm^{-2}. The band growths are ascribed to the increase of the concentration of Zr and N vacancies induced by electronic excitations inside tracks. For ceria, the decrease and broadening of the main F_{2g} peak of the fluorite-like structure and the growth of a broad defect band is observed versus fluence up to 10^{14} cm^{-2} for 200-MeV Xe ion irradiation. For YSZ, Raman spectra mainly give evidence of the intrinsic lattice disorder arising from the native oxygen vacancies, even up to high fluences (~$3x10^{13}$ cm^{-2}) for 200-MeV I and 200-MeV Au ion irradiation. Results are discussed on the basis of the interplay between the native structural disorder and the radiation-induced disorder by electronic excitation in those three materials.

KEYWORDS: Yttria-stabilized zirconia, ceria, zirconium nitride, swift heavy ion irradiation, Raman spectroscopy.

I. INTRODUCTION

Radiation damage in ceramics is a key issue for the nuclear energy applications. Among these materials, zirconium nitride (ZrN) [Takaki, 2016] and yttria-stabilized zirconia (ZrO_2: Y, or YSZ) [Matzke, 1999] are envisioned as important inert matrixes for transmutation of minor actinides. Those two ceramics can actually incorporate actinides to be used as fuels to reprocess the long-lived α-emitters. As for fuel-cladding metallic alloys, zirconium is used for its low neutron capture cross section. Besides, cerium dioxide or ceria (CeO_2) is considered as a surrogate of actinide dioxides with the same cubic fluorite-like structure, such as UO_2 [Shi, 2016] and PuO_2 [Weber, 1984].

Many experimental techniques such as XRD and TEM/STEM and so forth are currently applied to probe the radiation damage. Raman scattering was widely used to study the damage induced by swift heavy ion irradiation in non-amorphizable oxides, such as urania (UO_2) [Desgranges, 2011; Gutierrez, 2018], or amorphizable oxides, such as yttrium iron garnet ($Y_3Fe_5O_{12}$, or YIG) [Costantini, 2015]. Similar studies were also dedicated to carbides, either amorphizable, such as SiC [Sorieul, 2006], or non-amorphizable, such as TiC and ZrC [Pellegrino, 2019]. Different kinds of Raman spectra and behavior under irradiation were encountered in those ceramics depending on the chemical bonding and respective radiation resistance. More specifically, for amorphizable solids such as SiC or YIG, the crystal lattice phonon peaks of the crystal gradually vanish and new broad bands can appear owing to a new short-range order (SRO) in the amorphous phase [Sorieul, 2006; Costantini, 2015, 2021]. In contrast, for non-amorphizable materials such as urania [Desgranges, 2011; Gutierrez, 2018] or ceria [Ohara 2009; Graham 2018, Costantini 2017, 2019a], no striking modifications of the Raman spectra are recorded, yet broad defect bands are growing after ion irradiation. Even though those fluorite-structure oxides are not amorphizable, point defects are actually formed either by nuclear collisions or electronic excitations [Costantini, 2013].

For swift heavy ion irradiations, the damage also depends whether the electronic stopping power is higher or lower than the threshold stopping power for track formation. In this respect, it is interesting to compare the behavior of different ceramic materials for about the same electronic

stopping power to check their radiation resistance in similar conditions. Therefore, the scope of this paper was to use micro-Raman spectroscopy as a means to study the damage induced in those three ceramics of interest (YSZ, CeO_2, and ZrN) by swift heavy irradiations, in view to mimic the radiation effects of fission or spallation fragments. Raman spectra clearly highlight the behavior under ion irradiation of those three non-amorphizable ceramics with the cubic structure, but with different bonding character and different SRO arising from the native point defects. This gives insights on subtle modifications that are not easily available to other experimental techniques.

II. EXPERIMENTAL PROCEDURES

Ceria polycrystalline samples in thickness of 500 µm and with grain sizes of ~10 µm have been prepared by a sintering process at 1800 K for 12 h, then at 1700 K for 4 h. Zirconium nitride samples in thickness of 500 µm and with grain sizes of ~5 µm were also prepared by sintering at 1973 K for 6 h in a N_2 gas flow [Takaki, 2018]. Sintered samples were polished on one side. Irradiations were applied on the polished sides near room temperature (RT) with 100-MeV ^{131}Xe for ZrN and 200-MeV ^{131}Xe for CeO_2 at the Tokai Tandem accelerator (JAEA Ibaraki, Japan) up to fluences of $1x10^{12}$ cm^{-2} and $1x10^{14}$ cm^{-2}, respectively, with a flux of $\sim10^9$ cm^{-2} s^{-1}. Virgin CeO_2 samples were ivory in color then turned light green after irradiation, whereas ZrN samples kept their bright golden color. The YSZ single crystal plates, i.e. ZrO_2: Y (with 9.5 mol% Y_2O_3) with the <100> orientation and in thickness of 500 µm were supplied by Crystal-GmbH (Berlin, Germany). Irradiation of these single crystals was carried out with 200-MeV ^{127}I and 20-MeV ^{197}Au ions at the VIVITRON (Strasbourg, France) up to $3x10^{13}$ cm^{-2} also with a low flux (~10^8-10^{10} cm^{-2} s^{-1}) in order to prevent sample heating. Virgin YSZ samples were colorless and transparent then turned to a dark color for high fluences.

Irradiation parameters such as projected range (R_p) and stopping power are computed with the SRIM-2013 code [http://www.srim.org/] (Table I). The nuclear collision (S_n) and electronic stopping powers (S_e) are plotted versus depth (Fig. 1). Close S_e values are found for the incident energies in the three compounds (Table I).

Micro-Raman spectra were recorded at room temperature (RT) between 100 and 1800 cm^{-1} for virgin and irradiated samples in a backscattering geometry using an Invia Reflex® Renishaw spectrometer coupled with an Olympus microscope containing an *x-y-z* stage. Measurements were performed on the virgin sample and samples irradiated at various fluences. The (non-polarized) 532-nm line of a frequency-doubled Nd-YAG laser was focused on a 1 x 1 μm^2 spot and collected through a 100 × objective. The laser power was kept below 1 mW to avoid in-beam sample annealing. The TO/LO peak at 521 cm^{-1} of a silicon wafer was used as a reference. All spectra for each kind of materials were recorded in exactly the same conditions of laser power and exposure time. Several spectra were recorded on different spots to check the homogeneity of samples.

UV-visible measurements of ZrN were conducted in the diffuse reflection mode using a Praying Mantis™ Diffuse Reflection accessory mounted on a Perkin-Elmer Lambda-1050® spectrometer. Spectra were recorded from 200 to 2500 nm (~0.5 to 5 eV in photon energy) at RT for virgin and irradiated samples with a focal spot of ~1 mm averaging the collected light over ~200 grains. An Teflon powder was used as a blank reference. Similar diffuse UV-visible reflectivity measurements were already carried out on CeO_2 sintered samples [Costantini, 2019a].

III. RESULTS AND DATA ANALYSIS

Raman spectra of virgin and irradiated YSZ, CeO_2 and ZrN are displayed for the various fluences (Figs. 2-4). Homogeneous spectra are recorded for the YSZ single crystal plates, whereas some minor differences in peak intensities are found between grains for sintered ceria samples. Spectra of ZrN look inhomogeneous between the dark and clear zones at the sample surface. The spectra of the clear zones show the same bands but are broadened with respect to the dark zones.

The estimated probed depth of d ~2.3 µm in CeO_2 by Raman spectroscopy relies on the absorbance at RT of a 1-µm thick epitaxial film at the wavelength of 532 nm, for 63% attenuation of the scattered light [Costantini, 2019b]. However, this value is definitely overestimated owing to light scattering at grain boundaries of the sintered samples. This means that mainly the topmost part of

the irradiated depth was probed. An estimate of the probed depth (d) is also deduced for YSZ from the UV-visible absorption spectrum of a 500-µm thick single crystal plate at RT [Costantini, 2010]. The YSZ single crystal plates are actually transparent to the laser beam with a transmittance of 73% (absorbance of ~0.14) and absorption coefficient of α ~2.8x10^{-4} µm^{-1} at 532 nm [Costantini, 2010]. This yields a probed depth of d = 1/α ~3.6 mm, for 63% attenuation of the scattered light, which means that the whole sample thickness was probed in that case. The difference in probed depths for the photon energy of $\hbar\omega$ = 2.33 eV lies in the difference in optical gap of ~4.2 eV [Costantini, 2010] and ~3.2 eV [Costantini, 2019 ab], and Urbach edge for YSZ and CeO_2 respectively. The estimate of the probed depth by Raman spectroscopy in CeO_2 is marked by a vertical line in the depth profiles (Fig. 1).

Raman spectra of YSZ show a broad scattering continuum with two prominent peaks at ~150 and ~615 cm^{-1} (Fig. 2). The virgin sample spectrum is fitted with nine Gaussian profiles centered at 107, 150, 190, 227, 310, 384, 470, 582, and 617 cm^{-1}, with FWHMs ranging between 30 cm^{-1} for the band at 617 cm^{-1} to 140 cm^{-1} for the bands at 227, 384 and 582 cm^{-1}. All bands are kept after irradiation regardless of ion fluence. No striking radiation effect is found except for an overall flattening out of the scattered intensity for both ion irradiations. No broadening of the bands is deduced from fits for those high fluences (~3x10^{13} cm^{-2}) (Fig. 2). A decrease of band intensities by a factor ranging between ~2 and 3 is found for both ion irradiations. A greater decay of the band at 617 cm^{-1} is observed for the Au ion irradiation.

Raman spectra of ceria exhibit a prominent narrow peak at ~465 cm^{-1} and five small satellite peaks (Fig. 3, semi-log scale). The virgin spectrum is fitted with a Lorentzian peak centered at 467 cm^{-1} (Γ = 6.5 cm^{-1}) and five narrow Gaussian profiles of equal amplitudes and equal widths (FWHM ~5 cm^{-1}), centered at 493, 512, 523, 537, and 555 cm^{-1} (Fig. 3). For the low fluence (3x10^{11} cm^{-2}), only a slight decrease in intensity by ~8%, whereas the satellite peak intensities decrease by a factor of ~2, with no broadening of those peaks (Fig. 3). For the high fluence (10^{14} cm^{-2}), a decrease of the main peak intensity by a factor of ~42% is found with a clear decay of the satellite peak intensities by a

factor of ~10 (Fig. 3). For this fluence, a broadening of the main peak (Γ = 8.5 cm^{-1}) and merging with the first satellite at 493 cm^{-1} is observed, yet by keeping the Lorentzian shape centered at 467 cm^{-1}. However, no change in FWHMs of the satellite peaks is deduced from fits. For this fluence, a broad extra band has grown at ~600 cm^{-1} (marked with an arrow, Fig. 3).

The diffuse reflectivity spectra of ZrN show a strong decrease of reflectance for photon energies above ~3.2 eV, i. e. below ~390 nm (Fig. 4a), which is consistent with literature data [Karlsson, 1982; Lamni, 2004; Larijani, 2014] and the yellow color of samples [Kim, 2011; Niyomsoan, 2002]. An additional diffuse reflectivity spectrum is displayed for a virgin $Zr_{0.7}Dy_{0.3}N$ sintered sample with a small redshift of the absorption edge to ~2.8 eV and a more greenish color. The spectra without normalization were treated with the Kubelka-Munk (K-M) function or re-emission factor (F) (Fig. 4b) devised for thick samples in which self-absorption and scattering are significant [refs]:

$$F(\hbar\omega) = \frac{[1-R(\hbar\omega)]^2}{2R(\hbar\omega)} = \frac{\alpha(\hbar\omega)}{S} \qquad (1)$$

where R is the reflectance in %, and S is the scattering factor. This function is relevant for the case of a two-layer sample with an irradiated zone of 7 µm and non-irradiated material underneath. In this approximation, the reflection and scattering by the rear side of the sample is neglected. The spectra show similar shapes except for three extra absorption bands at ~0.5, 1, and 1.4 eV for ZrDyN (Fig. 4b). For the 532-nm laser line at 2.33 eV, the absorbance deduced from all those spectra is quite weak. A skin depth of ~73 µm in ZrN is obtained for the corresponding electromagnetic radiation of the 532-nm laser line with the frequency of 5.63 MHz, a resistivity of 12 µΩ cm at 300 K, and a relative permeability of 1. This means that the whole irradiated depth of 7 µm was probed by Raman scattering.

No clear and significant radiation effects are observed on the absorption spectra (Fig. 4b) in the present conditions except for changes in intensity strongly depending on the sample surface state and experimental conditions. The Raman spectra (Fig. 5) exhibit broad bands that are fitted

with eight Gaussian profiles centered at 165, 225, 335, 402, 455, 510, 650, and 710 cm^{-1} (Fig. 5). The integrated intensities of the four prominent bands at ~165, 225, 455, and 510 cm^{-1} clearly grow with ion fluence with no change in the FWHMs of ~50, 55, 35 and 115 cm^{-1}, respectively.

IV. DISCUSSION

IV.1 ZIRCONIA AND CERIA

Both Zr and Ce dioxides are insulating ionic-covalent materials. The Zr–O phase diagram is quite complex [Etsell, 1970; Feinberg, 1981]. The stable phase of ZrO_2 at RT is monoclinic (α-ZrO_{2-x}) for ~67 O at% with little oxygen deficiency. The tetragonal ZrO_2 phase (β-ZrO_{2-x}) is stable between ~1000°C and 1200°C, whereas cubic zirconia (γ-ZrO_{2-x}) is stable only above ~1550°C within a wide domain of oxygen deviation to stoichiometry expanding with temperature up to ~62 O at%, i. e. x ~0.07, below the melting point (2710 °C in normal conditions) [Etsell, 1970]. Owing to the small tetragonal distortion of the unit cell (c/a = 1.02) [Etsell, 1970], it is not easy to differentiate the β and γ phases by X-ray diffraction (XRD) powder patterns. In order to stabilize the cubic fluorite-like phase at RT, substitution of Y^{3+} for Zr^{4+} is widely used for Y_2O_3 contents larger than ~9 mol%, corresponding to a critical oxygen vacancy concentration (~10 at%) produced by charge compensation of Y^{3+} ions [Zacate, 2000]. Two Y^{3+} ions (Y_{Zr}') are compensated by one oxygen vacancy with the 2+ charge state ($V_O^{\cdot\cdot}$). Partial stabilization can also occur for lower yttria contents [ref].

The cubic phase of yttria-stabilized zirconia (YSZ, ZrO_{2-x}: Y^{3+}) exhibits an atomic disorder due the large amount of vacancies, even though XRD patterns of polycrystalline samples are interpreted with a cubic fluorite-like phase [Michel, 1976]. This is clearly reflected by the Raman spectrum of an YSZ single crystal with 9.5 mol% yttria showing a broad scattering continuum with several maxima (Fig. 2). This spectrum is similar to Raman data of highly-doped gadolinia-stabilized zirconia (GSZ, ZrO_{2-x}: Gd^{3+}), calcia-stabilized zirconia (CSZ, ZrO_{2-x}: Ca^{2+}), and magnesia-stabilized zirconia (ZrO_{2-x}: Mg^{2+}) [Michel, 1976]. Such spectra partly derive from the folding of the total phonon density-of-states (DOS) at the center of the first Brillouin zone, instead of specific optical phonon branches

intersecting the Γ point (for q = 0), due to the breakdown of the selection rules for Raman scattering in a disordered solid [Brodsky, 1978].

The contribution of low-frequency modes is actually seen, e. g. the peaks at 107 and 150 cm^{-1}, like for highly-doped CSZ or GSZ [Michel, 1976], even though these low-frequency modes are normally not Raman-active in the periodic crystal. Such kind of broad continuum was also seen for amorphous solids, e. g. amorphous silicon or germanium [Tauc, 1976]. The ordering of oxygen vacancies can occur after annealing at high temperatures (~1000°C) giving rise to well-defined Raman peaks of an ordered phase, e. g. for CSZ [Michel, 1976].

Nine bands are deduced from the fits of spectra for the virgin and irradiated YSZ samples (Fig. 2). The peak at 617 cm^{-1} on top of the broad background can be assigned to the Raman-active F_{2g} (or triply degenerate T_{2g}) mode of the fluorite structure (Fig. 2). The Gaussian shape of this peak reflects the intrinsic disorder in this solid.

Such a peak is also found for ceria at 467 cm^{-1} with the five small satellite peaks at 493, 512, 523, 537, and 555 cm^{-1} which can be assigned to the oxygen deficiency [Nakajima, 1994, McBride, 1994, Dohčević-Mitrović, 2007, Kainbayev, 2020] (Fig. 3). The second-order and overtone peaks above 650 cm^{-1} are not shown. In contrast to YSZ, it has a sharp and narrow Lorentzian shape instead of a Gaussian shape, since CeO_2 has a stable cubic fluorite phase at RT with a small deviation to oxygen stoichiometry. Like YSZ, the domain of stability of the CeO_{2-x} phase for ~67 O at% at RT also expands with temperature up to ~62 O at%, i. e. x ~0.07, below the melting point (2293°C in normal conditions) [Sørensen, 1981].

The peak shift in wave number derives from the mass difference between Zr and Ce atoms, since heavier oscillators have actually lower vibration frequencies. For urania, with heavier U atoms, the F_{2g} zone-center phonon was found for a lower Raman shift of 448 cm^{-1} [Graves, 1990]. Comparison of Raman spectra for both oxides clearly shows a striking difference of the SRO at the level of bonds, even though they have both the same cubic fluorite-like structure.

Despite the uncertainties of the fits, the five bands centered at 150, 227, 310, 470, and 617 cm^{-1} for YSZ (Fig. 2) may be tentatively assigned to the following Raman-active modes of the tetragonal phase of ZrO_2 doped with Y^{3+} at 155 (B_{1g}), 266 (E_g), 326 (B_{1g}), 474 (E_g), and 616 (A_{1g}) cm^{-1} [Feinberg, 1981; Bouvier, 2001]. However, there is no evidence of the high-frequency phonon (E_g) mode at 645 cm^{-1} in the present spectra. The two broad bands at 384 and 582 cm^{-1} may be assigned to the TO IR-active A_{2u} (365 cm^{-1}) and E_u (575 cm^{-1}) modes, respectively, of the tetragonal phase of ZrO_2 doped with Y^{3+} [Bouvier, 2001] that can become allowed by disorder. The last two low-frequency bands at 107 and 190 cm^{-1} cannot be ascribed to optical modes of the tetragonal or cubic zirconia, but rather to two A_g optical modes (103 and 190 cm^{-1}) of the monoclinic phase [Zhao, 2001], or to the TA-LA acoustic modes near 10-14 meV (~80-113 cm^{-1}), as measured by inelastic neutron scattering of YSZ with 8-9 mol% Y_2O_3 [Cousland, 2014].

To summarize, the present Raman spectra of YSZ samples mainly show the contributions of: i) the symmetrical (g) optical modes of the cubic, and tetragonal phases, ii) anti-symmetrical (u) optical modes of the tetragonal phase, and/or iii) acoustic modes of the cubic phase. This likely arises from a partial stabilization of the cubic phase and folding of the phonon DOS to the center-of-zone due to lattice disorder. Actually the bands have broad Gaussian shapes (Fig. 2), rather than Lorentzian shapes like for ceria, owing to the structural disorder induced by the large amount of oxygen vacancies. The disorder induced by radiation damage results in a flattening of all bands for both ion irradiations.

Those spectra of YSZ and ceria do not exhibit drastic modifications after swift heavy ion irradiations, since they are both radiation-resistant materials that cannot be amorphized by track overlap [Costantini, 2013; Yasuda, 2020]. Even though tracks are not amorphous, threshold electronic stopping power values for track formation ($S_{e,t}$) in the energy range of ~1 MeV u^{-1} (Table 1, marked with dotted horizontal lines, Fig. 1) were deduced from experimental data combined with simulations with the inelastic thermal spike (i-TS) model for YSZ [Costantini, 2007a; Moll, 2009] and ceria [Costantini, 2017]. For the present ion irradiations, it is found that $S_e > S_{e,t}$ over a depth of ~5 to

10 µm (Fig. 1). Moreover, the stopping power depth profiles in CeO_2 and ZrO_2 show that the contribution of nuclear collisions can be overlooked over the whole ion range (Fig. 1).

Raman spectra of ceria sintered samples show a maximum decrease by 45% of the F_{2g} peak for the highest fluence of Xe ions (10^{14} cm^{-2}) (Fig. 3), whereas a maximum decrease by ~60% is observed for YSZ for the high fluence of Au ions ($2.5x10^{13}$ cm^{-2}) (Fig. 2). For YSZ, there is an overall flattening out of the whole scattered signal, keeping the same broad bands as the virgin material with no significant broadening of all bands for both ions at high fluences of ~$3x10^{13}$ cm^{-2}. A similar decrease of band intensities is found for both ions, except for a larger decay of the F_{2g} peak for Au ion irradiation. Radiation damage in ceria also induces a clear decay of the satellite peaks by a factor of ~10 and without any broadening for the highest fluence (Fig. 3). The growth of a broad band at ~600 cm^{-1} (tagged with an arrow, Fig. 3) was assigned to point defect formation, most likely oxygen vacancies [Ohhara, 2009]. This is consistent to STEM/HAADF results showing the presence of oxygen vacancies in the track core of ceria for 200-MeV Xe ion irradiation [Takaki, 2016]

At most, a polygonized structure was observed in ion-irradiated YSZ [Costantini, 2008], which is similar to that of UO_2 [Matzke, 2000]. The maximum disorder fraction was of f_D^{max} ~40% in YSZ after swift heavy ion irradiations, as measured by RBS/C spectroscopy [Costantini, 2007a]. For ceria, a value of f_D^{max} ~45% was deduced from the decrease of the F_{2g} peak intensity as a function of fluence, after swift heavy ion irradiations [Costantini, 2017]. As such, ceria and YSZ reach similar f_D^{max} values. However, the main difference between those two oxides lies in the MRO and the amount of oxygen vacancies at RT, even though the deviation to stoichiometry in ceria and YSZ reaches similar values at high temperature before melting. It is liable to consider that the high-temperature atomic structure of both materials is quite similar. However, simulations with the i-TS model for the same range of ion energy ~1 MeV u^{-1} gave a higher threshold value of ~20 keV nm^{-1} for YSZ [Moll, 2009] than for ceria ($S_{e,t}$ ~6 keV nm^{-1}) [Costantini, 2017]. Experimental RBS/C data for YSZ found that 18 keV nm^{-1} < $S_{e,t}$ < 24 keV nm^{-1} [Costantini, 2007a].

Raman spectra show that the disorder level in YSZ is enhanced after ion irradiation even though it is challenging to assess it from Raman spectra (Fig. 2). Actually, the main origin of disorder in this material is related to the native oxygen vacancies, regardless of the damage induced by irradiation which is limited by the high recombination rate of radiation-induced defects in the oxygen sub-lattice by the native oxygen vacancies [Devanathan, 2008]. Molecular dynamics (MD) simulations have actually shown that a recoiling oxygen atom of 200 eV cannot displace oxygen atoms in YSZ [Costantini, 2011], in good agreement with the large threshold displacement energy (E_d) of oxygen [Costantini, 2007b]. As a result, the intrinsic chemical disorder clearly overweighs in the Raman spectra the radiation-induced disorder in YSZ, in contrast to CeO_2 with a small oxygen deficiency.

IV.2 **ZIRCONIUM NITRIDE**

Stoichiometric ZrN has a cubic rock salt structure (B1, Fm3m space group) and is considered to have a metallic bonding character [Yu, 2017; Patsalas, 2019]. The samples indeed show a metallic lustre with a golden color. Raman spectra exhibit broad bands that can be fitted by Gaussian profiles which can be assigned to acoustic TA mode at 165 cm^{-1} and LA mode at 225 cm^{-1}, and optical TO modes at 455 cm^{-1} and LO modes at 510 cm^{-1} [Saha, 2010; Mokgadia, 2019] with a TO–LA phonon gap of ~230 cm^{-1} between them (Fig. 4). The intermediate bands at 335 and 402 cm^{-1} are assigned to 2TA and (TA + LA) overtones, respectively [Saha, 2010; Mokgadia, 2019]. Two more bands are recorded at 650 and 710 cm^{-1} which may be assigned to (TO + LA) or (LO + LA) combination modes, respectively. Several second-order (two-phonon) modes were also recorded above 900 cm^{-1}, i. e. at ~1000 (2LO), 1315 (2(TO + LA)), and 1455 cm^{-1} (2(LO + LA)) (not shown). The Gaussian shape of all broad bands also reflects the intrinsic disorder just like for YSZ.

Like for ZrC_{1-x} and TiC_{1-x}, [Pellegrino, 2019], that are also metallic compounds [Jubair, 2019], the TA and LA modes appear in Raman spectra due to the disorder arising from the nitrogen deficiency in ZrN_{1-x}. Those bands should be strictly forbidden by Raman selection rules in periodic solids but they become Raman-allowed owing to the lattice disorder [Brodsky, 1978]. This is a clear

experimental evidence of the non-stoichiometry of the samples. The acoustic modes were associated to Zr vacancies, whereas the optical modes were associated to N vacancies [Saha, 2010]. The integrated peak intensities (I) of the TA, LA and (TO + LO) bands increase with the 100-MeV Xe ion fluence (φ) according to a saturation law (Fig. 5, inset):

$$I = I_0 + (I_\infty - I_0)\,(1 - e^{-\sigma\varphi}) \qquad (2)$$

where I_0 is the virgin sample intensity, I_∞ is the asymptotic value, and σ is a damage cross section. Least-square fits with Eq. 2 yield similar σ values of 1.77×10^{-12} cm^2 for the (TO + LO) band, 1.44×10^{-12} cm^2 for the LA band, and 8.81×10^{-13} cm^2 for the TA band. The TA and LA bands have the same kind of behavior, whereas the increase ($I_\infty - I_0$) of the (TO + LO) band is larger. Even though cross sections are similar, the difference by a factor of ~2 in the growth ($I_\infty - I_0$) of TA/LA and TO/LO bands is consistent with the higher formation energy of Zr vacancies than N vacancies [Ivanovskii, 2001]. More N vacancies are produced than Zr vacancies upon irradiation.

The effect of irradiation is also seen on the TO–LO mode resolution which diminishes with irradiation. This is related to the accumulation of point defects enhancing the disorder. The TO and LO bands are merging owing to the broadening of bands due to increasing disorder. A similar broadening effect is seen on the TA and LA acoustic modes, but to a smaller extent. This is likely an ion track effect for a high electronic stopping power in this low fluence range with damage cross sections σ of ~1.5×10^{-12} cm^2, giving a track diameter of D ~13.8 nm. It is seen that no amorphization is induced in ZrN_{1-x} like for ZrC_{1-x} and TiC_{1-x}, [Pellegrino, 2019].

This is consistent with the absorption spectra (Fig. 4b) showing no clear changes with irradiation. No significant shift or smearing of the broad absorption band peaking at ~3.5 eV is observed. Significant changes are instead found for the Dy doping. This absorption band is corresponding to the screened plasmon frequency (at ~3.2 eV) [Kim, 2011]. The absorbance includes

contribution of conduction electrons (Drude term) and bound electrons (Lorentz term) giving an asymmetrical shape to this band [Schlegel, 1977; Valerini, 2010; Kim, 2011].

MD simulations by the two-temperature model (so-called i-TS model) have actually evidenced the formation of isolated vacancies in the tracks of bcc metals, such as W for S_e = 60 keV nm^{-1} [Khara, 2017]. Self-interstitials are accumulated at the center of the track cores and form prismatic dislocation loops after recrystallization of the molten zone. Vacancies are formed and trapped at the border of the recrystallization front. A similar process of vacancy formation by electronic excitation is likely in the present case of ZrN for a high S_e value, provided that melting occurs in the track core for S_e = 26 keV nm^{-1}. The melting point, which is a key factor in this process, is similar for ZrN (2980°C) and for W (3422°C) in normal conditions. A lower damage was found for Fe because of a lower melting point (1538°C) than W [Khara, 2017]. Even though the stopping power is lower, the lattice thermal conductivity of ZrN (κ = 20 W m^{-1} K^{-1}) is much smaller than that of W (κ = 164 W m^{-1} K^{-1}). This may compensate for the difference in input energy to reach the melting point in tracks. However, simulations with the i-TS model would be necessary to ascertain this point. The $S_{e,t}$ value for ZrN is not available to the best of our knowledge.

A small track diameter of D = 1.23 $\pm$ 0.12 nm was deduced from the lattice parameter expansion after 200-MeV Xe ion irradiation for S_e= 30.7 keV nm^{-1} [Takaki, 2018]. The XRD data actually show that ZrN is not amorphized by such irradiation up to the fluence of 10^{14} cm^{-2} in agreement with our results. The material is keeping the rock-salt structure, even though the Bragg peaks are clearly broadened by the accumulation of point defects generating internal lattice strain [Takaki, 2018]. The discrepancy on track diameter with the present results is often encountered when comparing different techniques such as XRD, TEM/STEM, optical absorption spectroscopy and so forth. Similar deviations in track radii were already found for the non-amorphous tracks in CeO_2 [Costantini, 2017; 2019b] and amorphous ones in YIG [Costantini, 2015]. The present determination of D ~14 nm for ZrN is consistent with the value of D ~10 nm for CeO_2 [Costantini, 2017] and D ~12

nm for YIG [Costantini, 2015], for the same stopping power of S_e = 26 keV nm^{-1} and the same range of ion velocity (~1 MeV u^{-1}).

Radiation effects of 167-MeV Xe ions for a similar stopping power but for a much larger fluence (6.77x10^{14} cm^{-2}) were reported for ZrN layers in thickness of 20 µm deposited on a silicon substrate. From their Raman spectra, *Mokgadia et al.* have concluded to a weak damage induced by the 167-MeV Xe ions, owing to the low energy loss by nuclear collisions of Xe ions with respect to 200-keV Eu ion implantation to a fluence of 1x10^{16} cm^{-2} [Mokgadia, 2019]. This is clearly a variance with the present results since the saturation of Raman band growth occurs for a much lower fluence, which cannot be related to displacement damage. In the latter case, a linear increase versus fluence would have been expected in this range of low fluence. This saturation corresponds instead to the full track overlap.

Full-cascade simulations were carried out with the SRIM-2013 computer code [http://www.srim.org/] for ~10^5 ions with E_d(Zr) = 33 eV and E_d(N) = 29 eV [Rahman, 2021]. The total number of vacancies per ion is of N ~6.3x10^4. An excess of Zr vacancies is obtained over N vacancies (Fig. 1), owing to the larger displacement cross section for about the same E_d values. For φ = 3x10^{12} cm^{-2} at the saturation, it gives a total density of Zr and N vacancies of Nφ ~2x10^{16} cm^{-2}, i. e. a maximum number of displacement per atom of $\mathrm{dpa} = \frac{N\varphi}{N_a R_p}$ ~3.5x10^{-4}, where N_a = 8.12x10^{22} cm^{-3} is the average atomic density. As a result, the contribution of nuclear collisions cannot be completely discarded, but it is indeed very low, knowing that SRIM simulations overestimate the number of stable Frenkel pairs. Moreover, the differential increase in Zr and N vacancies (Fig. 4) is not compatible with the cascade simulations, since an excess of Zr vacancies is produced by nuclear collisions (Fig. 1). This is clearly at variance with the larger increase of N vacancies versus fluence with respect to Zr vacancies, as found from the present Raman data. This difference in point-defect production yields likely derives from ionization processes, rather than collisional processes.

The differences in microstructure and nitrogen deficiency between samples might account for the discrepancy with the results of *Mokgadia et al.* [Mokgadia, 2019]. Actually, Raman spectra of

Mokgadia et al. are showing degenerate TO and LO modes in the virgin sample spectrum [Mokgadia, 2019]. In our samples, the LO peak is much larger and broader than the TO peak with a ratio of LO/TO integrated intensities of ~10 (Fig. 4), in contrast to the data of *Mokgadia et al.* showing an inverted ratio [Mokgadia, 2019]. The merging of those two modes in the as-deposited films means a less polar bonding character than in the present sintered samples with a TO–LO splitting of 55 cm^{-1}. This experimental TO–LO splitting is smaller than the calculated splitting of 191 cm^{-1} by DFT-GGA theory [Saha, 2010]. For sake of comparison, TO and LO modes are degenerate at the center of zone (Γ point) in silicon [Seeger, 2004], with non-polar Si–Si bonding, whereas they are very well split by ~200 cm^{-1} in SiC [Sorieul, 2006]. Besides, the large TA–LA phonon gap is due to the large mass difference of Zr and N atoms. Large TA–LA and LA–TO phonon gaps were also found for ZrC_{1-x} and TiC_{1-x} with four well defined TA, LA, TO, and LO broad bands [Pellegrino, 2019]. In the latter two metallic materials, Raman spectra also derive from the presence of native carbon vacancies.

As a result, it looks like the bonding and the non-stoichiometry in the ZrN layers used by *Mokgadia et al.* was different from our polycrystalline samples. It is known that various compositions can be obtained in the Zr–N system for the same rock-salt structure, even the most stable over-stoichiometric Zr_3N_4, which is a semiconductor with a band-gap energy of 0.68 eV [Yu, 2017]. The bulk and shear moduli both exhibit a strong decrease as a function of the vacancy concentration [Yu, 2017], owing to the decrease of Zr-N covalent bonds, which may have an impact on the lattice response to irradiation.

In contrast to YSZ, with a large intrinsic disorder arising from the high concentration of native oxygen vacancies, the disorder induced by radiation damage in ZrN is quite well evidenced by Raman spectroscopy, despite broad bands. Raman scattering in such a metallic compound is rendered possible by the native nitrogen vacancies. However, the associated intrinsic disorder does not overshoot the extra disorder induced in tracks by ion irradiation which can be quantitatively assessed by Raman spectroscopy. In summary, these results on three different materials exemplify the

versatility as well as the limits of Raman spectroscopy in probing the disorder induced by heavy ion irradiation in ceramics with different native structural disorder and bonding character.

V. CONCLUSIONS

Raman spectroscopy is used to study the damage induced by swift heavy ion irradiation in three ceramics, namely ZrO_2: Y (YSZ), CeO_2 and ZrN with different bonding and different intrinsic structural disorder, for about the same high electronic stopping power. Those three compounds are radiation-resistant materials in which ion-track accumulation does not lead to amorphization. However, point defects are formed and can leave an imprint on the Raman spectra provided that the intrinsic structural disorder does not overshadow the disorder induced by irradiation.

For ZrN, Zr and N vacancy accumulation is evidenced from the growth of the TA/LA and TO/LO bands versus fluence up to saturation for $3x10^{12}$ cm^{-2} for 100-MeV Xe ion irradiation. For CeO_2, the formation of oxygen vacancies is deduced from the growth of a defect band for 200-MeV Xe ion irradiation. A decrease and broadening of the main F_{2g} peak of the cubic fluorite structure is also evidenced with increasing fluence up to 10^{14} cm^{-2}. For YSZ, the effect of 200-MeV I ion irradiation is overweighed by the intrinsic disorder arising from the large oxygen vacancy content. Raman spectra only reflect the intrinsic disorder of native vacancies up to a high fluence ($3x10^{13}$ cm^{-2}). The defect formation in those ceramics is attributed to electronic excitation processes.

References

[Bouvier, 2001] P. Bouvier, H. C. Gupta, and G. Lucazeau, J. Phys. Chem. Solids **62** (2001) 873

[Brodsky, 1978] M. H. Brodsky, and M. Cardona, J. Non-Crystal. Solids **31** (1978) 81

[Costantini, 2007a] J. M. Costantini, C. Trautmann, L. Thomé, J. Jagielski, and F. Beuneu, J. Appl. Phys., **101** (2007) 073501

[Costantini, 2007b] J. M. Costantini, and F. Beuneu, Phys. Stat. Sol. (c) **4** (2007) 1258

[Costantini, 2008] J. M. Costantini, F. Guillet, S. Lambert, D. Grébille, F. Beuneu, and C. Trautmann, J. Appl. Phys. **104** (2008) 073504

[Costantini, 2010] J. M. Costantini, F. Beuneu, K. Schwartz, and Christina Trautmann, J. Phys.: Condens. Matter **22** (2010) 315402

[Costantini, 2011] J. M. Costantini, F. Beuneu, S. Morrison-Smith, R. Devanathan, and W. J. Weber, J. Appl. Phys. **110** (2011) 123506

[Costantini, 2013] J. M. Costantini, F. Beuneu, and W. J. Weber, "*Radiation Damage in Cubic-Stabilized Zirconia and Ceria*", in "*Properties of Fluorite Structure Materials*", P. Vajda and J. M. Costantini Eds. (Nova Science Publishers, New York, 2013), Chapter 5.

[Costantini, 2015] J. M. Costantini, S. Miro, F. Beuneu, and M. Toulemonde, J. Phys.: Condens. Matter **27** (2015) 496001

[Costantini, 2017] J.-M. Costantini, S. Miro, G. Gutierrez, K. Yasuda, S. Takaki, N. Ishikawa, and M. Toulemonde, J. Appl. Phys. **122** (2017) 205901

[Costantini, 2019a] J.-M. Costantini, G. Lelong, M. Guillaumet, D. Gourier, S. Takaki, N. Ishikawa, H. Watanabe, and K. Yasuda, J. Appl. Phys. **126** (2019) 175902

[Costantini, 2019b] J.-M. Costantini, G. Gutierrez, H. Watanabe, K. Yasuda, S. Takaki, G. Lelong, M. Guillaumet, and W. J. Weber, Philos. Mag. **99** (2019) 1695

[Costantini, 2021] J. M. Costantini, Phil. Mag. Lett. **101** (2021) 185

[Cousland, 2014] G.P. Cousland, R. A. Mole, M. M. Elcombe, X. Y. Cui, A. E. Smith, C. M. Stampfl, A. P. J. Stampfl, J. Phys. Chem. Solids **75** (2014) 351

[Desgranges, 2011] L. Desgranges, G. Baldinozzi, P. Simon, G. Guimbretière, and A. Canizares, J. Raman Spectrosc. **43** (2012) 455

[Devanathan, 2008] R. Devanathan, and W. J. Weber, J. Mater. Res. **23** (2008) 593

[Etsell, 1970] T. H. Etsell, and S. N. Flengas, Chem. Reviews **70** (1970) 339

[Feinberg, 1981] A. Feinberg, and C. H. Perry, J. Phys. Chem. Solids **42** (1981) 513

[Graham 2018] J.T. Graham, Y. Zhang, and W.J. Weber, J. Nucl. Mater. **498** (2018) 400

[Graves, 1990] P. R. Graves, Appl. Spectrosc. **44** (1990) 1665

[Gutierrez, 2018] G. Gutierrez, C. Onofri , S. Miro , M. Bricout , F. Leprêtre, Nucl. Instr. and Meth. B **434** (2018) 45

[Jubair, 2019] M. Jubair, A. M. M. Tanveer Karim, M. Nuruzzaman, and M. A. K. Zilan, J. Phys. Commun. **3** (2019) 055017

[Ivanovskii, 2001] A. L. Ivanovskii, N. I. Medvedeva, and S. V. Okatov, Inorganic Materials **37** (2001) 552

[Karlsson, 1982] B. Karlsson, R. P. Shimshock, and B. 0. Seraphin, Physica Scripta. **25** (1982) 775

[Khara, 2017] G. S Khara, S. T. Murphy, and D. M Duffy, J. Phys.: Condens. Matter **29** (2017) 285303

[Kim, 2011] J. Kim, S.-H. Jhi, and K. R. Lee, J. Appl. Phys. **110** (2011) 083501

[Lamni, 2004] R. Lamni, E. Martinez, S. G. Springer, R. Sanjinés, P. E. Schmid, and F. Lévy, Thin Solid Films **447–448** (2004) 316

[Larijani, 2014] M. M. Larijani, M. Kiani, E. Jafari-Khamse, and V. Fathollahi, Appl. Phys. A **117** (2014) 1179

[Matzke, 1999] Hj. Matzke, V. V. Rondinella, and T. Wiss, J. Nucl. Mater. **274** (1999) 153151

[Matzke, 2000] Hj. Matzke, P. G. Lucuta, and T. Wiss, Nucl. Instr. and Meth. B **166/167** (2000) 634

[Michel, 1976] D. Michel, M. Perez Y Jorba, and R. Collongues, J. Raman Spectrosc. **5** (1976) 163

[Mokgadia, 2019] T. F. Mokgadia, M. J. Maditob, M. Mlamboa, V. A. Skuratovc, S.V. Motloung, and T. T. Hlatshwayo, Nuclear Inst. and Methods B **461** (2019) 63

[Moll, 2009] S. Moll, L. Thomé, L. Vincent, F. Garrido, G. Sattonnay, T. Thomé, J. Jagielski, and J. M. Costantini, J. Appl. Phys. **105** (2009) 023512

[Niyomsoan, 2002] S. Niyomsoan, W. Grant, D.L. Olson, B. Mishra, Thin Solid Films **415** (2002) 187

[Ohhara, 2009] K. Ohhara, N. Ishikawa, S. Sakai, Y. Matsumoto, O. Michikami, and Y. Ohta, Nucl. Instr. and Meth. B **267** (2009) 973

[Patsalas, 2019] P. Patsalas, Thin Solid Films **688** (2019) 137438

[Pellegrino, 2019] S. Pellegrino, P. Trocellier, L. Thomé, S. Miro, J-M. Costantini, and E. Jouanny, Nuclear Inst. and Methods B **454** (2019) 61

[Rahman, 2021] M. M. Rahman, T. Yamamoto, S. Matsumura, J-.M. Costantini, and K.Yasuda, J. Nucl. Mater. (2021)

[Saha, 2010] B. Saha, J. Acharya,T. D. Sands,and U. V. Waghmare, J. Appl. Phys. **107** (2010) 033715

[Schlegel, 1977] A. Schlegel, P. Wachter, J. J. Nicklt and H Lingg, J. Phys. C: Solid State Phys., **10** (1977) 4889

[Seeger, 2004] K. Seeger, "*Optical Absorption and Reflection*", in "*Semiconductor physics: an introduction*" (Springer, Berlin, 2004), Chapter 11, p 356

[Shi, 2016] L. Shi, E. Vathone, V. Olson, M. Freyss, and R. Hayn, Phys. Rev. B **94** (2016) 115132

[Sorieul, 2006] S. Sorieul, J. M. Costantini, L. Gosmain, G. Calas, J. J. Grob, and L. Thomé, J. Phys.: Condens. Matter **18** (2006) 5235

[Sørensen, 1981] O. T. Sørensen, in "*Nonstoichiometric Oxides*", O. T. Sørensen Editor (Academic, New York, 1981).

[Takaki, 2016] S. Takaki, K. Yasuda, T. Yamamoto, S. Matsumura, and N. Ishikawa, Progress in Nucl. Energy **92** (2016) 306

[Takaki, 2018] S. Takaki, and N. Ishikawa, Progress in Nucl. Energy **5** (2018) 204

[Tauc, 1976] J. Tauc, in "*Physics of Structurally Disordered Solids*", Ed. S. S. Mitra (Plenum, New York, 1976)

[Valerini, 2010] D. Valerini, M. A. Signore, A. Rizzo, and L. Tapfer, J. Appl. Phys. **108** (2010) 083536

[Weber, 1984] W. J. Weber, Radiation Effects **83** (1984) 145

[Yasuda, 2020] K. Yasuda, J.-M. Costantini, and G. Baldinozzi, "*Radiation-induced Effects on Materials Properties of Ceramics: Mechanical and Dimensional Properties*", in "*Comprehensive Nuclear Materials*", 2nd edition (2020)

[Yu, 2017] S. Yu, Q. Zeng, A. R. Oganov, G. Frapper, B. Huang, H. Niuc; and L. Zhang, RSC Adv. 7 (2017) 4697

[Zacate, 2000] M. O. Zacate, L. Minervini, D. J. Bradfield, R. W. Grimes, and K. E Sickafus, Solid State Ion. **128** (2000) 243

[Zhao, 2001] X. Zhao, and D. Vanderbilt, Phys. Rev. B **65** (2001) 075105

Table I: Irradiation parameters of CeO_2, ZrO_2, and ZrN with mass density ρ: mean projected range (R_p), electronic stopping power (S_e), and nuclear stopping power (S_n) for ions at the incident energy E computed with the SRIM-2013 code [*http://www.srim.org/*], and threshold stopping power ($S_{e,t}$) for track formation in CeO_2 [Costantini, 2017] and YSZ [Moll, 2009] in this range of ion energy (E/A).

Material	ρ (g cm^{-3})	$S_{e,t}$ (keV nm^{-1})	Ion	E (MeV)	E/A (MeV u^{-1})	R_p (µm)	S_e (keV nm^{-1})	S_n (keV nm^{-1})	S_e/S_n
CeO_2	7.215	~6	^{131}Xe	200	1.53	11.8 ± 0.6	27.3	0.113	241
ZrO_2: Y	5.81	20	^{127}I	200	1.57	12.7 ± 0.6	26.1	0.097	269
ZrO_2: Y	5.81	20	^{197}Au	200	1.01	11.3 ± 0.6	32.3	0.029	1113
ZrN	7.09		^{131}Xe	100	0.76	6.9 ± 0.5	26.1	0.21	124

Figure 1: Depth profiles of the electronic stopping power (S_e including the ionization by recoils in the end-of-range region) (dashed curves) and nuclear stopping power (S_n) (solid curves) computed with the SRIM-2013 code [*http://www.srim.org/*] for CeO_2, ZrN, and ZrO_2 (left scale). The numbers of Zr ($N(V_{Zr})$) and N vacancies ($N(V_N)$) per ion and per nm in ZrN are deduced from the full cascade simulations (right scale). The probed depth in CeO_2 is shown with a dotted vertical line, and the threshold electronic stopping powers ($S_{e,t}$) for track formation in YSZ (red) and CeO_2 (black) are shown with horizontal dotted lines.

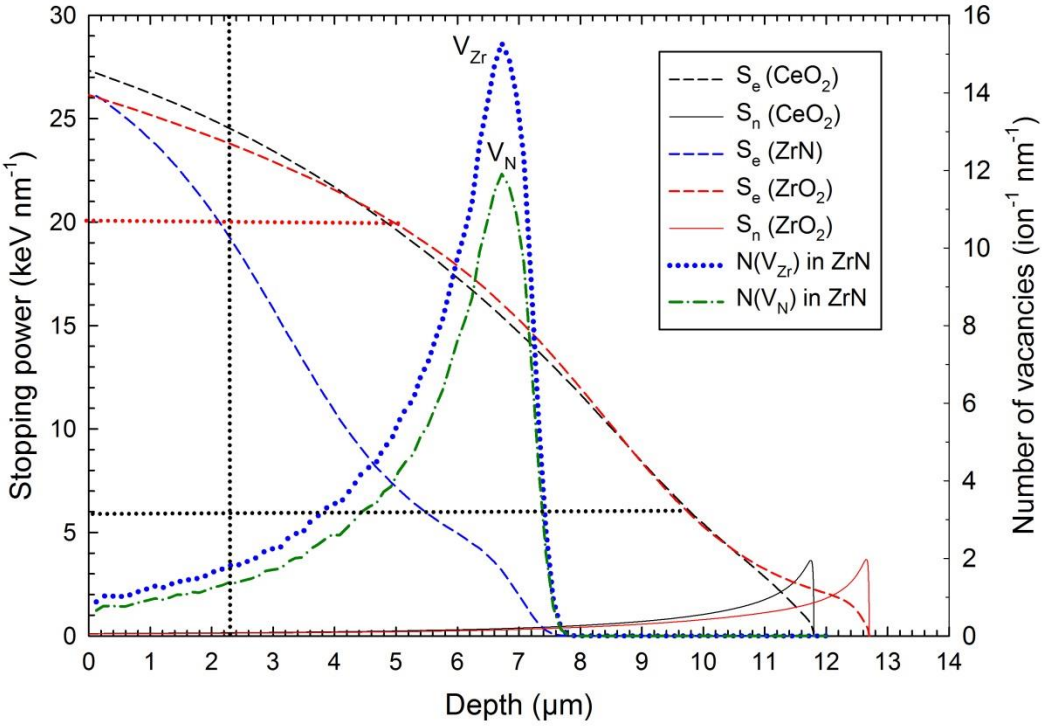

Figure 2: Raman spectra of virgin and irradiated YSZ single crystals (with 9.5 mol% yttria) for 200-MeV I and 200-MeV Au ions. The dotted curves are fits with the nine Gaussian profiles shown for the virgin sample (dashed curves). The bands are assigned according to the phonon modes of the monoclinic (m), tetragonal (t), and cubic (c) ZrO_2 phases.

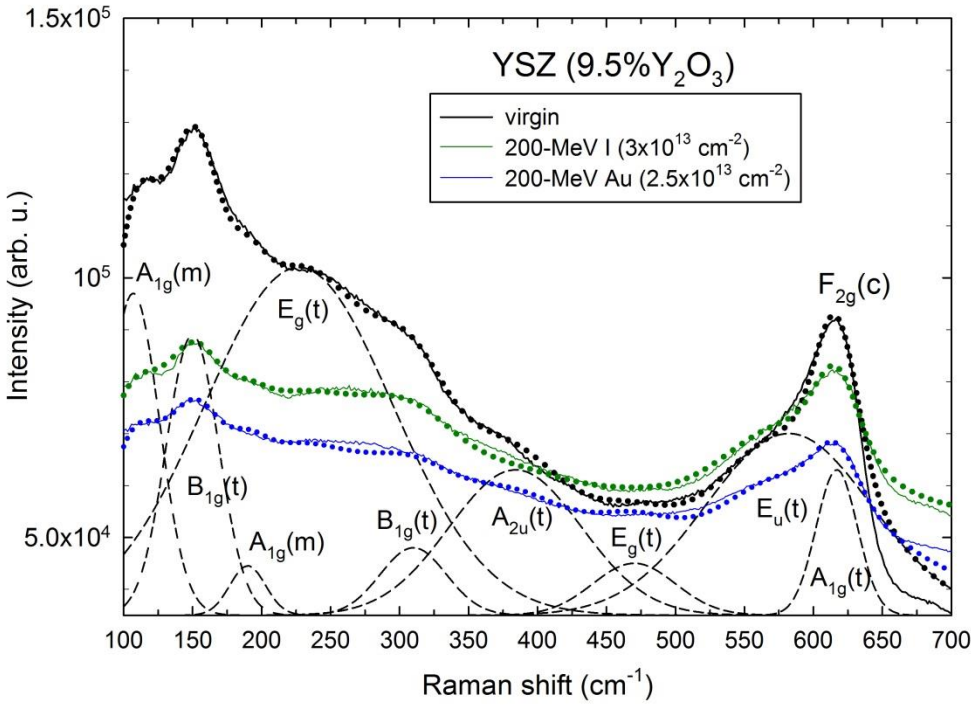

Figure 3: Raman spectra of virgin and irradiated ceria sintered samples for two fluences of 200-MeV Xe ions. The dotted curves are fits with one Lorentzian profile for the F_{2g} peak and five Gaussian profiles for the satellites. The defect band at ~600 cm^{-1} is tagged with an arrow.

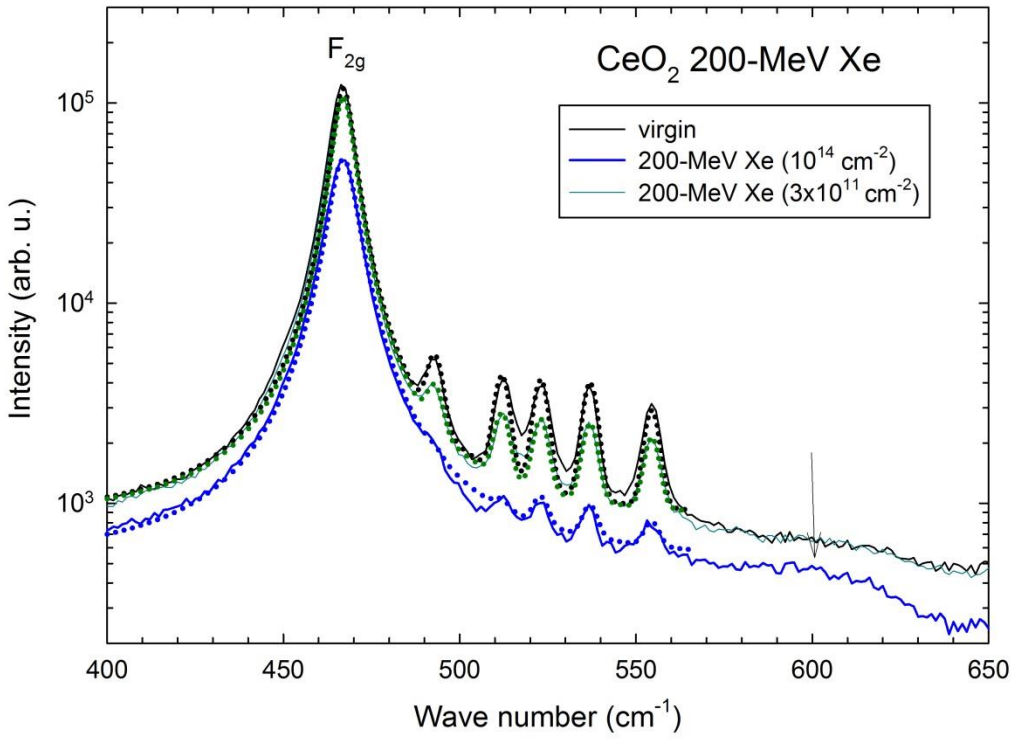

Figure 4: UV-visible diffuse reflectance spectra (a) and re-emission factor (F) (b) as a function of photon energy for virgin ZrN and ZrDyN samples and irradiated ZrN samples for two fluences of 100-MeV Xe ions.

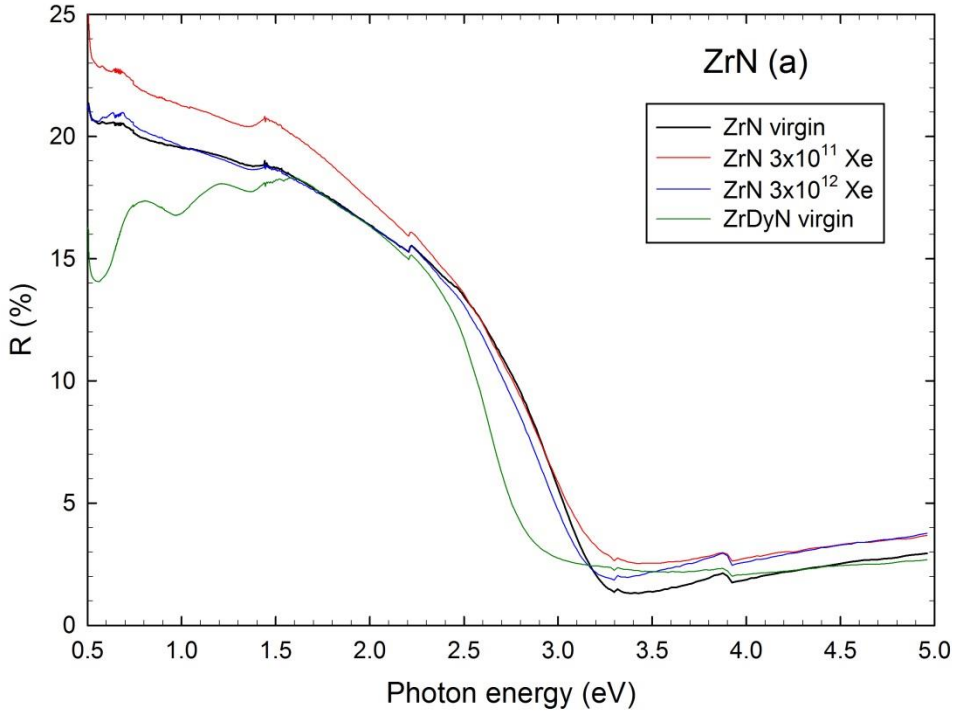

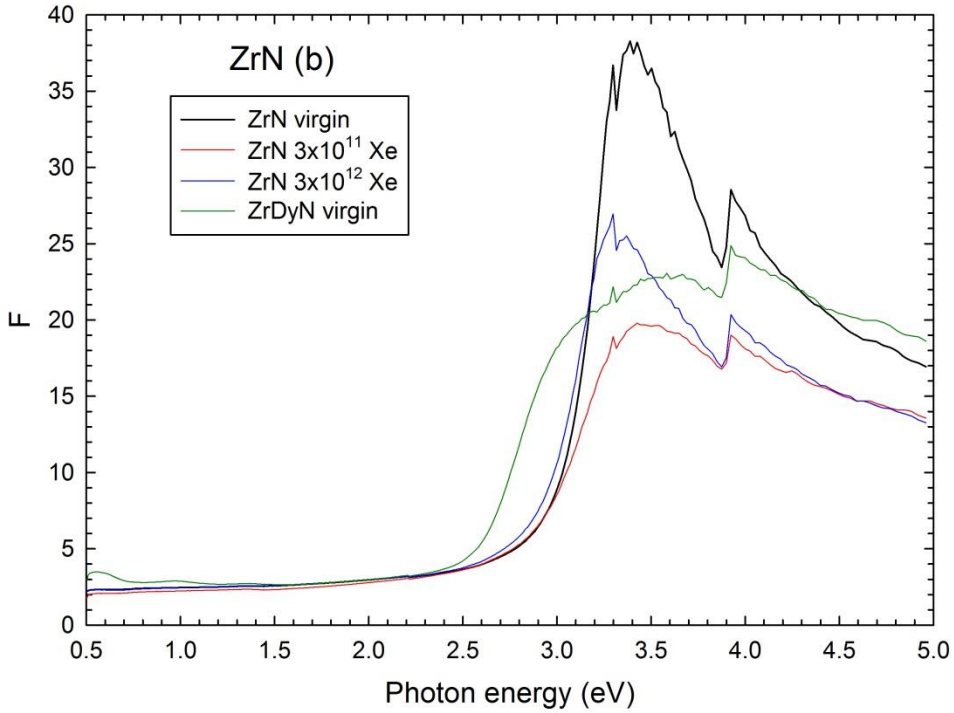
ZrN (b)
ZrN virgin
ZrN 3x10^11 Xe
ZrN 3x10^12 Xe
ZrDyN virgin
F
Photon energy (eV)
0
5
10
15
20
25
30
35
40
0.5
1.0
1.5
2.0
2.5
3.0
3.5
4.0
4.5
5.0

Figure 5: Raman spectra of virgin and irradiated ZrN sintered samples for the two fluences of 100-MeV Xe ions. Dotted curves are the fits with the eight Gaussian profiles shown for the virgin sample (dashed curves) with assignments to the phonon modes of ZrN. Inset: band integrated intensities for the TA, LA and TO + LO bands as a function of ion fluence.